Weaker cooling by aerosols due to dust-pollution interactions

Klaus Klingmüller[1], Vlassis A. Karydis[2], Sara Bacer[3], Georgiy L. Stenchikov[4], and Jos Lelieveld[1,5]

[1]Max Planck Institute for Chemistry, Hahn-Meitner-Weg 1, 55128 Mainz, Germany
[2]Forschungszentrum Jülich GmbH, IEK-8, 52425 Jülich, Germany
[3]LEGI, Université Grenoble Alpes, CNRS, Grenoble INP, Grenoble, France
[4]King Abdullah University of Science and Technology, Thuwal 23955-6900, Saudi Arabia
[5]The Cyprus Institute, P.O. Box 27456, 1645 Nicosia, Cyprus

Correspondence: Klaus Klingmüller (k.klingmueller@mpic.de)

Abstract.

The interactions between aeolian dust and anthropogenic air pollution, notably chemical ageing of mineral dust and coagulation of dust and pollution particles, modify the atmospheric aerosol composition and burden. Since the aerosol particles can act as cloud condensation nuclei, this not only affects the radiative transfer directly via aerosol-radiation interactions, but also indirectly through cloud adjustments. We study both radiative effects using the global ECHAM/MESSy atmospheric chemistry-climate model (EMAC) which combines the Modular Earth Submodel System (MESSy) with the European Centre/Hamburg (ECHAM) climate model. Our simulations show that dust-pollution interactions reduce the cloud water path and hence the reflection of solar radiation. The associated climate warming outweighs the cooling which the dust-pollution interactions exert through the direct radiative effect. In total, this results in a net warming by dust-pollution interactions which moderates the negative global anthropogenic aerosol forcing at the top of the atmosphere by $(0.2 \pm 0.1)\ \mathrm{Wm}^{-2}$.

1 Introduction

A prime objective of current atmospheric and climate science is the deeper understanding of ambient aerosols and their interactions with clouds. This is motivated by their central role in two areas of societal importance, public health and climate change. The inhalation of aerosols allows fine particles to enter deep into the respiratory system or even translocate through the lungs into the cardiovascular system causing a multitude of health challenges, and making the exposure to fine particulate air pollution one of the main public health risks worldwide (Lelieveld et al., 2015, 2019a, b; Chowdhury et al., 2020). On the other hand, aerosols modify the albedo of the Earth, predominantly increasing the reflection of solar radiation and thus cooling the planet. Since the emissions of anthropogenic greenhouse gases are accompanied by those of anthropogenic aerosols, to a large extent through common source categories, the greenhouse warming has been partially masked by the aerosol effects on climate (IPCC, 2014; Lelieveld et al., 2019a).

The planetary albedo can be increased both directly by interactions of the anthropogenic aerosol particles with solar radiation and indirectly by enhanced cloudiness or cloud brightness caused by aerosol particles acting as cloud condensation nuclei.

Atmospheric
Chemistry
and Physics
Discussions
Open Access
EGU

These direct and indirect effects are estimated to contribute a negative effective radiative forcing (ERF) of -0.45 $\mathrm{Wm^{-2}}$ each, adding up to about -0.9 $\mathrm{Wm^{-2}}$ (IPCC, 2014).

Since not all aerosols in the atmosphere are of anthropogenic origin – in fact natural aerosols including aeolian dust and sea salt are the most abundant components by mass – the anthropogenic pollutants form a mixture with natural aerosols.

5 On the one hand particulate pollution coagulates with natural particles and on the other hand natural particles are exposed to chemical ageing. Klingmüller et al. (2019) showed that the interactions between natural mineral dust and anthropogenic pollution enhance the global net-cooling through the direct radiative effects and have a significant impact on regional radiative transfer. Here we extend the analysis to include the indirect radiative effects. The abundant atmospheric water vapour represents a vast source of cloud water so that cloud optical depths are typically much larger than aerosol optical depths. Therefore, cloud

10 adjustments potentially leverage the aerosol radiative effect and we may expect the indirect radiative effect of the dust-pollution interactions to be even more significant than the direct effect.

We use the global ECHAM/MESSy atmospheric chemistry-climate model (EMAC) which combines the Modular Earth Submodel System (MESSy) with the European Centre/Hamburg (ECHAM) climate model. It includes implementations of an extensive set of relevant physical and chemical processes, including detailed parametrisations of mineral dust ageing, cloud

15 droplet activation and ice crystal formation in cirrus and mixed-phase clouds.

The model and its configuration are described in Sect. 2 followed by an outline of the methodology of our analysis in Sect. 3. Results for the dust-pollution interaction effect on the cloud condensate are presented in Sect. 4, and the resulting effects on radiative transfer in Sect. 5. Conclusions are presented in Sect. 6.

2 Model description

20 The EMAC model version and configuration used in the present study are largely identical to those used by Klingmüller et al. (2018, 2019), combining ECHAM 5.3.02 and MESSy 2.52. However, to allow decadal simulations, the horizontal resolution has been reduced to a Gaussian T63 grid with a grid spacing of $1.875°$ along latitudes and about $1.86°$ along longitudes, corresponding to an edge length of the individual grid cells of around 200 km or less. The number of vertical levels remains at 31. Moreover, the present study uses the EDGARv4.3 (Emissions Database for Global Atmospheric Research) database

25 for anthropogenic emissions (Crippa et al., 2016) and a backport of the CLOUD submodel from MESSy 2.54 to benefit from recent improvements of the cloud parametrisations.

As in the previous studies, the GFEDv3.1 (Global Fire Emissions Database) (Randerson et al., 2013) and AeroCom (Aerosol Comparisons between Observations and Models) (Dentener et al., 2006) databases provide biomass burning and sea salt emissions, respectively. Mineral dust emissions are calculated online by the submodel ONEMIS (Kerkweg et al., 2006b) using the

30 dust emission scheme presented by Klingmüller et al. (2018) which is based on Astitha et al. (2012). It differentiates the $\mathrm{Ca^{++}}$, $\mathrm{K^+}$, $\mathrm{Mg^{++}}$ and $\mathrm{Na^+}$ fractions in mineral particles originating from different deserts (Karydis et al., 2016).

The MESSy submodels most relevant for aerosols include the Global Modal Aerosol Extension (GMXe) (Pringle et al., 2010a, b). It simulates the microphysics of four soluble (nucleation, Aitken, accumulation, coarse) and three insoluble (Aitken,

accumulation, coarse) aerosol log-normal modes with fixed geometric standard deviations ($\sigma_\mathrm{g} = 2$ for the coarse modes, $\sigma_\mathrm{g} =$ 1.59 for all others). The count median dry radius of each mode can vary between fixed boundaries at 6 nm, 60 nm and 1 μm. Super coarse mineral dust particles are therefore only included as part of the coarse modes with mean radius larger than 1 μm and their mass is probably underrepresented (Adebiyi and Kok, 2020). However, their role in the dust-pollution-

5 cloud interactions is limited by their low number concentration, corresponding to a low probability for pollution particles to coagulate with them, and a comparably short atmospheric residence time, leaving less time for chemical ageing. Within GMXe, the gas-aerosol partitioning can be computed by ISORROPIA II (Fountoukis and Nenes, 2007) or EQSAM4clim (Equilibrium Simplified Aerosol Model V4 for climate simulations) (Metzger et al., 2016), here we use ISORROPIA II. Assuming diffusion limited condensation, it calculates the amount of gas kinetically able to condense using the accommodation coefficients in

10 Table S1 in the supplement. Subsequently the mass is re-distributed between gas and aerosol phase to obtain the amount of condensed material (Pringle et al., 2010a, b).

   Insoluble particles are transferred to the soluble modes if sufficient soluble material has condensed to cover the particles with 10 molecular monolayers, or if they coagulate with soluble particles (Vignati et al., 2004; Stier et al., 2005; Pringle et al., 2010a, b). In particular, freshly emitted mineral dust is assumed to be hydrophobic and thus emitted into the insoluble

15 aerosol modes (with approximately 89 %, the majority of the mass is emitted into the coarse mode and the remainder into the accumulation mode), but chemical ageing and coagulation can transfer the mineral dust particles to soluble modes allowing them to grow by taking up water and act as cloud condensation nuclei. The chemical ageing and partitioning of organic aerosol is implemented in the submodel ORACLE (Organic Aerosol Composition and Evolution) (Tsimpidi et al., 2014, 2018). GMXe and ORACLE interact with the gas phase whose chemistry is simulated by the submodel MECCA (Module Efficiently

20 Calculating the Chemistry of the Atmosphere) (Sander et al., 2019).

   The AEROPT (AERosol OPTical properties) submodel (Lauer et al., 2007; Klingmüller et al., 2014) calculates the aerosol optical properties assuming the aerosol components within each mode to be well mixed in spherical particles with volume averaged refractive index. The aerosol optical properties are considered by the radiative transfer submodel RAD (Dietmüller et al., 2016) to account for the aerosol-radiation coupling. In the solar spectrum, absorption and scattering are computed

25 using extinction coefficient, single scattering albedo and asymmetry parameter, whereas in the terrestrial spectrum scattering is neglected. The latter approximation is valid for particles much smaller than the wavelength and is therefore largely justified for the long terrestrial wavelengths, but might be inaccurate in the presence of super coarse particles (Di Biagio et al., 2020). However, this affects only the direct radiative effect which turns out to be far less relevant in the context of the present study than the indirect radiative effect.

30 Aerosol removal by wet deposition is calculated by the scavenging submodel SCAV (Tost et al., 2006a), dry deposition and sedimentation by the submodels DDEP and SEDI (Kerkweg et al., 2006a). The aerosol and in particular the mineral dust representation in EMAC have a proven track record (e.g., Abdelkader et al., 2015; Metzger et al., 2016; Abdelkader et al., 2017; Klingmüller et al., 2018; Brühl et al., 2018; Metzger et al., 2018; Ma et al., 2019), the dust aerosol optical depth is consistent with observations not only at visible wavelengths but also in the infrared at 10 μm (Klingmüller et al., 2018), indicating a

35 realistic particle size distribution.

Large-scale clouds are simulated by the submodel CLOUD (Jöckel et al., 2006) where different parametrisations of cloud droplet formation and ice nucleation are implemented. We use a two-moment stratiform cloud microphysics scheme (Lohmann et al., 1999, 2007; Lohmann and Kärcher, 2002) in combination with the UAF (Unified Activation Framework) cloud droplet activation parametrisation (Kumar et al., 2011; Karydis et al., 2011, 2017). For the ice crystal formation we use the compre-

5 hensive parametrisation for cirrus and mixed-phase clouds implemented by Bacer et al. (2018) based on Barahona and Nenes (2009). Convective clouds are calculated by the CONVECT submodel (Jöckel et al., 2006), where interactions with aerosols are not taken into account. CONVECT provides a choice of convection schemes (Tost et al., 2006b), and here we use the scheme of Tiedtke (1989) including modifications by Nordeng (1994). The optical properties of clouds which serve as input for the radiative transfer submodel RAD are computed by the submodel CLOUDOPT (Dietmüller et al., 2016). The model

10 yields a global annual mean cloud liquid water path around $80 \, \mathrm{g \, m^{-2}}$ (Table 1 and Table S3 in the supplement), which is well within the range of other climate model results (32 to $125 \, \mathrm{g \, m^{-2}}$, Lebsock and Su, 2014) and observations (30 to $90 \, \mathrm{g \, m^{-2}}$, Lohmann and Neubauer, 2018). Likewise, the modelled annual mean global cloud ice water path of about $15 \, \mathrm{g \, m^{-2}}$ (Table 1 and Table S3 in the supplement) is consistent with results from other models (e.g., $14.8 \, \mathrm{g \, m^{-2}}$, Lohmann and Neubauer, 2018) and close to observed values (e.g., $(25 \pm 7) \, \mathrm{g \, m^{-2}}$, Li et al., 2012).

15 A complete list of the MESSy submodels used in our simulations is provided in Table S2 in the supplement. Descriptions of each submodel and further references can be found online in the MESSy submodel list (MESSy 2020).

3 Methodology

To estimate the global aerosol ERF, we study the radiative fluxes in simulations with prescribed sea surface temperature (SST) and sea ice climatologies. The ERF accounts for rapid adjustments by radiative and dynamical feedbacks, whereas it excludes

20 long-term climate responses involving the much slower thermal equilibration of the oceans. Due to the limited constraints on the atmospheric dynamics in SST simulations, the meteorological variability is large and hence a sufficient number of years has to be simulated to obtain statistically significant results. We perform SST simulations long enough to yield significant globally averaged results, however detailed regional analysis would require much longer SST simulations. In order to nevertheless gain insights from regional evaluation, we additionally use simulations where the model dynamics above the boundary layer

25 is nudged to meteorological analyses of the European Centre for Medium-Range Weather Forecasts (ECMWF). Within the boundary layer and to some extend above, nudged quantities like the temperature may still respond to other variables such as radiative fluxes (soft nudging). The nudging greatly reduces the influence of inter-annual variability on statistical analysis. The results from the nudged simulations turn out to be largely consistent with those of the SST simulations (Tabs. 1, 2 vs. Tabs. S3, S4 in the supplement), in particular the estimates for the total global radiative effect of the dust-pollution interactions agree

30 within the error bounds, so that the use of nudged simulations for the regional analysis is reasonable and helpful.

With prescribed SST we run ensembles of 16 simulations, each covering one year. The ensemble members are obtained by perturbing temperature and humidity in the fourth year of a common spin-up simulation, followed by an additional spin-up of the individual ensemble members to attain a total of 5 spin-up years. The perturbation is implemented by adding a uniformly

Atmospheric
Chemistry
and Physics
Discussions

distributed random variable ranging from -0.1 ‰ to 0.1 ‰ of the perturbed quantity so that the perturbation is numerically but not meteorologically relevant. Emission data for 2010 is used for all simulations. The nudged simulations cover 10 years from 2006 to 2015, and two simulation years prior to that period were used for the model spin-up. To estimate the uncertainties of the 10-year mean values for the nudged simulations and the ensemble mean values for the SST simulations, we compute the

5 standard error of the mean of the annual values.

We apply a similar analysis as Klingmüller et al. (2019) which is based on simulations with four different emission set-ups: a baseline simulation with neither dust nor anthropogenic emissions ("0"), a simulation with dust but without anthropogenic emissions ("dust"), a simulation with anthropogenic pollution but without dust emissions ("pol") and a full simulation considering all emissions. Thus, in total we have performed four nudged simulations and four times 16 SST simulations.

10 In the anthropogenic pollution free simulations ("0", "dust") we disable the EDGAR emissions including SO_2, NH_3, NO_x, black- and organic carbon emissions, but retain the greenhouse gases. We attribute 90 % of the GFED biomass burning emissions to human activities (Levine, 2014) and reduce them accordingly, whereas we do not consider anthropogenic factors on dust emissions such as land use and climate change (Klingmüller et al., 2016), assuming all dust emissions to be natural.

A result x from the full simulation (e.g., the annual global mean cloud liquid water content) is related to the corresponding

15 result from the baseline simulation x_0 by

$$x = x_0 + \Delta_{\mathrm{dust}}x + \Delta_{\mathrm{pol}}x + \Delta_{\mathrm{int}}x \tag{1}$$

where $\Delta_{\mathrm{dust}}x = x_{\mathrm{dust}} - x_0$, $\Delta_{\mathrm{pol}}x = x_{\mathrm{pol}} - x_0$ and

$$\Delta_{\mathrm{int}}x = x - x_{\mathrm{dust}} - x_{\mathrm{pol}} + x_0, \tag{2}$$

which represents the effect of the dust-pollution interactions. In the absence of any interactions, the term $\Delta_{\mathrm{int}}x$ vanishes. We

20 apply Eq. (2) to the annual mean cloud liquid- and ice-water paths and radiative fluxes, both globally averaged and, only for the nudged simulations, per grid cell.

To compute the direct radiative effect of aerosols, the radiative transfer code is called twice for every model time step. The first call considers the aerosol-radiation interactions and is used to calculated the heating rates affecting the temperature, the second call ignores the aerosol-radiation interactions and computes the radiative fluxes and heating rates only for diagnostic

25 output. The difference of the radiative fluxes from both calls yields the instantaneous forcing due to the direct radiative effect of aerosols. Since both calls are performed with identical clouds, only little statistical noise is introduced by the strong variability of clouds. Nevertheless, in this way we obtain the direct radiative forcing in the presence of clouds, which is typically smaller than the clear sky forcing. The direct radiative forcing is subtracted from the total radiative forcing to extract the indirect radiative forcing of aerosols.

30 ## 4 Effects on the cloud condensate

Hydrophilic particulate anthropogenic pollution enhances the cloud droplet formation and thus the liquid water content (Table 1). However, in the presence of mineral dust particles this effect is reduced because fine pollution particles coagulate with

coarse dust particles decreasing the particle number and virtually cleaning the atmosphere from fine particulate pollution. Moreover, the adsorption activation of mineral dust particles occurs early on in the cloud formation process (Kumar et al., 2011), reducing the maximum supersaturation and inhibiting the activation of small pollution particles. These effects reduce the number of cloud condensation nuclei (Karydis et al., 2011, 2017) and decrease the cloud liquid water path as shown in
5 Fig. 1 (a). Especially over East and South Asia, where strong pollution emissions mix with aeolian dust from the Taklamakan, Gobi and Thar deserts, the reduction is substantial and regionally exceeds -40 $\mathrm{g\,m^{-2}}$. Even over polluted regions in Europe and the USA which are only occasionally exposed to dust intrusions, we obtain a small but significant reduction. This negative impact of the dust-pollution interactions over large parts of the northern hemisphere leads to a reduction of the global mean cloud liquid water path in Fig. 1 (a) by (-1.10 ± 0.03) $\mathrm{g\,m^{-2}}$. A comparable reduction by (-1.5 ± 0.2) $\mathrm{g\,m^{-2}}$ is obtained in
10 the SST simulations (Tab. 1). Relative to the mean liquid water path in the SST simulation considering all emissions (85.5 ± 0.1) $\mathrm{g\,m^{-2}}$, these reductions appear to be rather moderate. The reason is that the transport time periods between most of the major dust sources, especially the Sahara and the Middle East, and major pollution sources like Northern America and Europe to a large degree exceed the dust aerosol lifetime. In Asia these sources are less distant while pollution emissions are generally larger. Thus, the strong effects over Asia might provide an outlook for regions with emerging pollution sources close
15 to dust sources in Africa and the Middle East. But already today, due to the critical influence of clouds on radiative transfer, the relatively small changes of the water paths cause substantial radiative forcings as will be discussed in the next section.

The dust-pollution interaction effect on the cloud ice water path, shown in Fig. 1 (b), is less distinct. A negative impact is obtained over the Sahel. The direct radiative effect of mineral dust over the Sahara warms the atmosphere by absorption of solar radiation (Fig. S1 (a) in the supplement). This increases the atmospheric capacity to hold moisture and the vertical water
20 vapour transport (Fig. S1 (b) in the supplement). As a result, more moisture is available for ice cloud formation (Fig. S1 (c) in the supplement). Since the net direct radiative effect of the dust-pollution interactions cools the atmosphere over the Sahara (Klingmüller et al., 2019), it moderates the enhancement of ice cloud formation. A similar net cooling effect is found over the region around the Taklamakan and Gobi deserts. In this region with generally high ice water content, anthropogenic pollution enhances the ice water path, but adding dust reduces the number of anthropogenic ice nucleation particles via coagulation. In
25 contrast, a positive impact is obtained over coastal regions of Canada and Greenland around 60 degrees north, probably due to aerosol and cloud feedbacks on the polar and Ferrel cell circulations and associated vertical moisture transport. However, because of the comparably small radiative fluxes at these latitudes, this has relatively little impact on radiative fluxes from a global perspective. Due to the regionally varying sign of the dust-pollution interaction effect on cloud ice, the global mean in Fig. 1 (b) is close to zero, (-0.027 ± 0.003) $\mathrm{g\,m^{-2}}$. The corresponding value in the SST simulations, (-0.02 ± 0.03) $\mathrm{g\,m^{-2}}$, is
30 consistent with this result, being several orders of magnitude smaller than the global mean ice water path in the SST simulation considering all emissions, (14.70 ± 0.01) $\mathrm{g\,m^{-2}}$ (Tab. 1).

5 Radiative effects

The reduction of the cloud water content by dust-pollution interactions has a significant impact on the transfer of solar radiation ("shortwave", SW), which is shown in Fig. 2 (a). With reduced liquid cloud water, less solar radiation is reflected back to space resulting in a net positive forcing at the top of the atmosphere (TOA). Comparing Fig. 2 (a) and Fig. 1 (a) reveals the one-to-one

5   correspondence of the dust-pollution interaction effect on the liquid cloud water and solar radiation. Over the polluted regions of the northern hemisphere, i.e., Asia, Europe and North America, and over the Atlantic Ocean along the North African coast in the Saharan dust outflow, the positive forcing can exceed 2 $\mathrm{Wm^{-2}}$. Globally averaged, the net forcing in the solar spectrum shown in Fig. 2 (a) is (0.23 ± 0.01) $\mathrm{Wm^{-2}}$, the SST simulations yield an ERF of (0.3 ± 0.1) $\mathrm{Wm^{-2}}$ (Tab. 2).

On the other hand, the dust-pollution interaction effect on the terrestrial spectrum ("longwave", LW), Fig. 2 (b), is directly

10   related to the effects on ice clouds, Fig. 1 (b). This is most distinct over the Sahel, but also apparent over the East Asian deserts. The reduced cloud ice water path over these regions traps less outgoing terrestrial radiation resulting in a net cooling from the dust-pollution interactions. Over the Sahel the terrestrial TOA forcing reaches -2 $\mathrm{Wm^{-2}}$. With regard to the radiative energy budget, the regions with a significant dust-pollution interaction effect on cloud ice in Fig. 1 (b) are of different relevance. The Sahel, where the dust-pollution interactions reduce cloud ice, is relatively close to the equator and accordingly stronger

15   radiative fluxes are affected by the cloud ice changes than in the other regions, hence the global net radiative effect related to cloud ice is more relevant than the global net effect on cloud ice itself. Globally averaged, the net forcing in the terrestrial spectrum shown in Fig. 2 (b) is (-0.05 ± 0.01) $\mathrm{Wm^{-2}}$, and the SST simulations yield an ERF of (-0.08 ± 0.09) $\mathrm{Wm^{-2}}$ (Tab. 2).

Thus, a substantial positive forcing in the solar spectrum is partially compensated by a negative forcing in the terrestrial spectrum to yield a still considerable, positive net-forcing associated with the effect of dust-pollution interactions on clouds.

20   The global distribution of the total net-forcing at the TOA including the direct radiative effect is shown in Fig. 3. The regional forcing ranges from below -2 $\mathrm{Wm^{-2}}$ over the Sahel to above 2 $\mathrm{Wm^{-2}}$ over Asia. Even though overall these contributions partially counterbalance, with (0.15 ± 0.02) $\mathrm{Wm^{-2}}$ the corresponding global mean forcing in Fig. 3 is significantly positive. Consistently, the ERF in the SST simulations is (0.2 ± 0.1) $\mathrm{Wm^{-2}}$ (Tab. 2).

Figure 4 summarises the direct and indirect global TOA ERF of anthropogenic aerosol interacting with mineral dust and

25   in the absence of mineral dust, obtained from the SST simulations. Despite the more negative anthropogenic aerosol direct radiative forcing in the presence of mineral dust, already reported by Klingmüller et al. (2019), the effect of mineral dust on the total forcing is clearly dominated by the moderation of the indirect forcing. The figure highlights the importance of the dust-pollution interactions for assessing the cooling effect of anthropogenic aerosol: the cooling is substantially reduced by the interactions from (-0.81 ± 0.06) $\mathrm{Wm^{-2}}$ ERF, which is close to 0.9 $\mathrm{Wm^{-2}}$ estimated by IPCC (2014), down to $(-0.60 \pm$

30   $0.1)$ $\mathrm{Wm^{-2}}$.

6 Conclusions

We have studied the effects of interactions between mineral dust and anthropogenic pollution on clouds and radiation by comparing comprehensive global simulations performed with the atmospheric chemistry-climate model EMAC with several emission configurations.

5 The cloud water path is reduced by the dust-pollution interactions as they moderate the cloud water path increase caused by anthropogenic pollution. The reason for this moderation is that mineral dust particles decrease the number of anthropogenic cloud condensation nuclei by coagulation and additionally limit the activation of the fine hydrophilic anthropogenic particles by lowering the maximum supersaturation through adsorption activation. Dust-pollution interaction effects on the cloud ice content are noticeable as well, but less relevant.

10 The atmospheric radiative transfer is very sensitive to the reduction of the cloud water path. Generally, dust-pollution interactions affect the radiative transfer at all wavelengths (solar and terrestrial) by modifying both the direct aerosol-radiation interactions and the indirect radiative effect of aerosols via cloud adjustments. However, the total radiative effect of the dust-pollution interactions is dominated by the impact through the indirect effect which, in contrast to the direct effect, exerts an overall positive TOA net-forcing. The impact on the indirect radiative effect in turn is dominated by that on solar radiation

15 fluxes. In this case, the aforementioned decrease of the cloud water path reduces the cloud albedo and the reflection of solar radiation, resulting in a positive contribution to the radiative net-flux.

Our SST simulations show that dust-pollution interactions contribute (0.2 ± 0.1) $\mathrm{Wm^{-2}}$ to the global mean anthropogenic aerosol effective radiative forcing, significantly reducing the climate cooling effect of atmospheric aerosols. In view of this considerable contribution to the atmospheric energy balance, it is recommended to account for the dust-pollution interactions

20 in assessments of climate change especially because on a regional scale effects can be even larger. The net global effect partially depends on regionally counteracting positive and negative radiative forcings. This study emphasizes the importance of continued efforts to improve the understanding and parametrisations of the processes involved in order to reduce the uncertainty of future climate simulations.

Author contributions. KK performed the simulations assisted by VAK and SB, analysed the model results and wrote the article supported by JL, SB, VAK and GLS. All authors discussed the results and contributed to the final manuscript.

Competing interests. The authors declare that they have no conflict of interest.

Atmospheric
Chemistry
and Physics
Discussions

References

Abdelkader, M., Metzger, S., Mamouri, R. E., Astitha, M., Barrie, L., Levin, Z., and Lelieveld, J.: Dust–air pollution dynamics over the eastern Mediterranean, Atmospheric Chemistry and Physics, 15, 9173–9189, https://doi.org/10.5194/acp-15-9173-2015, 2015.

Abdelkader, M., Metzger, S., Steil, B., Klingmüller, K., Tost, H., Pozzer, A., Stenchikov, G., Barrie, L., and Lelieveld, J.: Sensitivity of
5   transatlantic dust transport to chemical aging and related atmospheric processes, Atmospheric Chemistry and Physics, 17, 3799–3821, https://doi.org/10.5194/acp-17-3799-2017, 2017.

Adebiyi, A. A. and Kok, J. F.: Climate models miss most of the coarse dust in the atmosphere, Science Advances, 6, eaaz9507, https://doi.org/10.1126/sciadv.aaz9507, 2020.

Astitha, M., Lelieveld, J., Abdel Kader, M., Pozzer, A., and de Meij, A.: Parameterization of dust emissions in the global atmospheric
10   chemistry-climate model EMAC: impact of nudging and soil properties, Atmospheric Chemistry and Physics, 12, 11 057–11 083, https://doi.org/10.5194/acp-12-11057-2012, 2012.

Bacer, S., Sullivan, S. C., Karydis, V. A., Barahona, D., Krämer, M., Nenes, A., Tost, H., Tsimpidi, A. P., Lelieveld, J., and Pozzer, A.: Implementation of a comprehensive ice crystal formation parameterization for cirrus and mixed-phase clouds in the EMAC model (based on MESSy 2.53), Geoscientific Model Development, 11, 4021–4041, https://doi.org/10.5194/gmd-11-4021-2018, 2018.

15   Barahona, D. and Nenes, A.: Parameterizing the competition between homogeneous and heterogeneous freezing in ice cloud formation – polydisperse ice nuclei, Atmospheric Chemistry and Physics, 9, 5933–5948, https://doi.org/10.5194/acp-9-5933-2009, 2009.

Brühl, C., Schallock, J., Klingmüller, K., Robert, C., Bingen, C., Clarisse, L., Heckel, A., North, P., and Rieger, L.: Stratospheric aerosol radiative forcing simulated by the chemistry climate model EMAC using Aerosol CCI satellite data, Atmospheric Chemistry and Physics, 18, 12 845–12 857, https://doi.org/10.5194/acp-18-12845-2018, 2018.

20   Chowdhury, S., Pozzer, A., Dey, S., Klingmueller, K., and Lelieveld, J.: Changing risk factors that contribute to premature mortality from ambient air pollution between 2000 and 2015, Environmental Research Letters, https://doi.org/10.1088/1748-9326/ab8334, 2020.

Crippa, M., Janssens-Maenhout, G., Dentener, F., Guizzardi, D., Sindelarova, K., Muntean, M., Van Dingenen, R., and Granier, C.: Forty years of improvements in European air quality: regional policy-industry interactions with global impacts, Atmospheric Chemistry and Physics, 16, 3825–3841, https://doi.org/10.5194/acp-16-3825-2016, 2016.

25   Dentener, F., Kinne, S., Bond, T., Boucher, O., Cofala, J., Generoso, S., Ginoux, P., Gong, S., Hoelzemann, J. J., Ito, A., Marelli, L., Penner, J. E., Putaud, J.-P., Textor, C., Schulz, M., van der Werf, G. R., and Wilson, J.: Emissions of primary aerosol and precursor gases in the years 2000 and 1750 prescribed data-sets for AeroCom, Atmospheric Chemistry and Physics, 6, 4321–4344, https://doi.org/10.5194/acp-6-4321-2006, 2006.

Di Biagio, C., Balkanski, Y., Albani, S., Boucher, O., and Formenti, P.: Direct Radiative Effect by Mineral Dust Aerosols Constrained by New
30   Microphysical and Spectral Optical Data, Geophysical Research Letters, 47, e2019GL086 186, https://doi.org/10.1029/2019GL086186, e2019GL086186 2019GL086186, 2020.

Dietmüller, S., Jöckel, P., Tost, H., Kunze, M., Gellhorn, C., Brinkop, S., Frömming, C., Ponater, M., Steil, B., Lauer, A., and Hendricks, J.: A new radiation infrastructure for the Modular Earth Submodel System (MESSy, based on version 2.51), Geoscientific Model Development, 9, 2209–2222, https://doi.org/10.5194/gmd-9-2209-2016, 2016.

35   Fountoukis, C. and Nenes, A.: ISORROPIA II: a computationally efficient thermodynamic equilibrium model for K^+-Ca^{2+}-Mg^{2+}-NH_4^+-Na^+-SO_4^{2-}-NO_3^--Cl^--H_2O aerosols, Atmospheric Chemistry and Physics, 7, 4639–4659, https://doi.org/10.5194/acp-7-4639-2007, 2007.

IPCC, ed.: Climate Change 2013 – The Physical Science Basis, Cambridge University Press, cambridge Books Online, 2014.

Jöckel, P., Tost, H., Pozzer, A., Brühl, C., Buchholz, J., Ganzeveld, L., Hoor, P., Kerkweg, A., Lawrence, M. G., Sander, R., Steil, B., Stiller, G., Tanarhte, M., Taraborrelli, D., van Aardenne, J., and Lelieveld, J.: The atmospheric chemistry general circulation model ECHAM5/MESSy1: consistent simulation of ozone from the surface to the mesosphere, Atmospheric Chemistry and Physics, 6, 5067–5104, https://doi.org/10.5194/acp-6-5067-2006, 2006.

Karydis, V. A., Kumar, P., Barahona, D., Sokolik, I. N., and Nenes, A.: On the effect of dust particles on global cloud condensation nuclei and cloud droplet number, Journal of Geophysical Research: Atmospheres, 116, D23 204, https://doi.org/10.1029/2011JD016283, 2011.

Karydis, V. A., Tsimpidi, A. P., Pozzer, A., Astitha, M., and Lelieveld, J.: Effects of mineral dust on global atmospheric nitrate concentrations, Atmospheric Chemistry and Physics, 16, 1491–1509, https://doi.org/10.5194/acp-16-1491-2016, 2016.

Karydis, V. A., Tsimpidi, A. P., Bacer, S., Pozzer, A., Nenes, A., and Lelieveld, J.: Global impact of mineral dust on cloud droplet number concentration, Atmospheric Chemistry and Physics, 17, 5601–5621, https://doi.org/10.5194/acp-17-5601-2017, 2017.

Kerkweg, A., Buchholz, J., Ganzeveld, L., Pozzer, A., Tost, H., and Jöckel, P.: Technical Note: An implementation of the dry removal processes DRY DEPosition and SEDImentation in the Modular Earth Submodel System (MESSy), Atmospheric Chemistry and Physics, 6, 4617–4632, https://doi.org/10.5194/acp-6-4617-2006, 2006a.

Kerkweg, A., Sander, R., Tost, H., and Jöckel, P.: Technical note: Implementation of prescribed (OFFLEM), calculated (ONLEM), and pseudo-emissions (TNUDGE) of chemical species in the Modular Earth Submodel System (MESSy), Atmospheric Chemistry and Physics, 6, 3603–3609, https://doi.org/10.5194/acp-6-3603-2006, 2006b.

Klingmüller, K., Steil, B., Brühl, C., Tost, H., and Lelieveld, J.: Sensitivity of aerosol radiative effects to different mixing assumptions in the AEROPT 1.0 submodel of the EMAC atmospheric-chemistry–climate model, Geoscientific Model Development, 7, 2503–2516, https://doi.org/10.5194/gmd-7-2503-2014, 2014.

Klingmüller, K., Pozzer, A., Metzger, S., Stenchikov, G. L., and Lelieveld, J.: Aerosol optical depth trend over the Middle East, Atmospheric Chemistry and Physics, 16, 5063–5073, https://doi.org/10.5194/acp-16-5063-2016, 2016.

Klingmüller, K., Metzger, S., Abdelkader, M., Karydis, V. A., Stenchikov, G. L., Pozzer, A., and Lelieveld, J.: Revised mineral dust emissions in the atmospheric chemistry–climate model EMAC (MESSy 2.52 DU_Astitha1 KKDU2017 patch), Geoscientific Model Development, 11, 989–1008, https://doi.org/10.5194/gmd-11-989-2018, 2018.

Klingmüller, K., Lelieveld, J., Karydis, V. A., and Stenchikov, G. L.: Direct radiative effect of dust–pollution interactions, Atmospheric Chemistry and Physics, 19, 7397–7408, https://doi.org/10.5194/acp-19-7397-2019, 2019.

Kumar, P., Sokolik, I. N., and Nenes, A.: Cloud condensation nuclei activity and droplet activation kinetics of wet processed regional dust samples and minerals, Atmospheric Chemistry and Physics, 11, 8661–8676, https://doi.org/10.5194/acp-11-8661-2011, 2011.

Lauer, A., Eyring, V., Hendricks, J., Jöckel, P., and Lohmann, U.: Global model simulations of the impact of ocean-going ships on aerosols, clouds, and the radiation budget, Atmospheric Chemistry and Physics, 7, 5061–5079, https://doi.org/10.5194/acp-7-5061-2007, 2007.

Lebsock, M. and Su, H.: Application of active spaceborne remote sensing for understanding biases between passive cloud water path retrievals, Journal of Geophysical Research: Atmospheres, 119, 8962–8979, https://doi.org/10.1002/2014JD021568, 2014.

Lelieveld, J., Evans, J. S., Fnais, M., Giannadaki, D., and Pozzer, A.: The contribution of outdoor air pollution sources to premature mortality on a global scale, Nature, 525, 367–371, https://doi.org/10.1038/nature15371, 2015.

Lelieveld, J., Klingmüller, K., Pozzer, A., Burnett, R. T., Haines, A., and Ramanathan, V.: Effects of fossil fuel and total anthropogenic emission removal on public health and climate, Proceedings of the National Academy of Sciences, 116, 7192–7197, https://doi.org/10.1073/pnas.1819989116, 2019a.

Lelieveld, J., Klingmüller, K., Pozzer, A., Pöschl, U., Fnais, M., Daiber, A., and Münzel, T.: Cardiovascular disease burden from ambient air pollution in Europe reassessed using novel hazard ratio functions, European Heart Journal, 40, 1590–1596, https://doi.org/10.1093/eurheartj/ehz135, 2019b.

Levine, J.: 5.5 - Biomass Burning: The Cycling of Gases and Particulates from the Biosphere to the Atmosphere, in: Treatise on Geo-
5   chemistry (Second Edition), edited by Holland, H. D. and Turekian, K. K., pp. 139 – 150, Elsevier, Oxford, second edition edn., https://doi.org/10.1016/B978-0-08-095975-7.00405-8, 2014.

Li, J.-L. F., Waliser, D. E., Chen, W.-T., Guan, B., Kubar, T., Stephens, G., Ma, H.-Y., Deng, M., Donner, L., Seman, C., and Horowitz, L.: An observationally based evaluation of cloud ice water in CMIP3 and CMIP5 GCMs and contemporary reanalyses using contemporary satellite data, Journal of Geophysical Research: Atmospheres, 117, D16105, https://doi.org/10.1029/2012jd017640, 2012.

10   Lohmann, U. and Kärcher, B.: First interactive simulations of cirrus clouds formed by homogeneous freezing in the ECHAM general circu-lation model, Journal of Geophysical Research: Atmospheres, 107, AAC 8–1–AAC 8–13, https://doi.org/10.1029/2001JD000767, 2002.

Lohmann, U. and Neubauer, D.: The importance of mixed-phase and ice clouds for climate sensitivity in the global aerosol–climate model ECHAM6-HAM2, Atmospheric Chemistry and Physics, 18, 8807–8828, https://doi.org/10.5194/acp-18-8807-2018, 2018.

Lohmann, U., Feichter, J., Chuang, C. C., and Penner, J. E.: Prediction of the number of cloud droplets in the ECHAM GCM, Journal of
15   Geophysical Research: Atmospheres, 104, 9169–9198, https://doi.org/10.1029/1999JD900046, 1999.

Lohmann, U., Stier, P., Hoose, C., Ferrachat, S., Kloster, S., Roeckner, E., and Zhang, J.: Cloud microphysics and aerosol indirect effects in the global climate model ECHAM5-HAM, Atmospheric Chemistry and Physics, 7, 3425–3446, https://doi.org/10.5194/acp-7-3425-2007, 2007.

Ma, J., Brühl, C., He, Q., Steil, B., Karydis, V. A., Klingmüller, K., Tost, H., Chen, B., Jin, Y., Liu, N., Xu, X., Yan, P., Zhou, X., Abdelrahman,
20   K., Pozzer, A., and Lelieveld, J.: Modeling the aerosol chemical composition of the tropopause over the Tibetan Plateau during the Asian summer monsoon, Atmospheric Chemistry and Physics, 19, 11 587–11 612, https://doi.org/10.5194/acp-19-11587-2019, 2019.

MESSy 2020: MESSy submodel list, http://www.messy-interface.org/current/auto/messy_submodels.html, visited 1 April 2020.

Metzger, S., Steil, B., Abdelkader, M., Klingmüller, K., Xu, L., Penner, J. E., Fountoukis, C., Nenes, A., and Lelieveld, J.: Aerosol water parameterisation: a single parameter framework, Atmospheric Chemistry and Physics, 16, 7213–7237, https://doi.org/10.5194/acp-16-
25   7213-2016, 2016.

Metzger, S., Abdelkader, M., Steil, B., and Klingmüller, K.: Aerosol water parameterization: long-term evaluation and importance for climate studies, Atmospheric Chemistry and Physics, 18, 16 747–16 774, https://doi.org/10.5194/acp-18-16747-2018, 2018.

Nordeng, T.-E.: Extended versions of the convective parametrization scheme at ECMWF and their impact on the mean and transient activity of the model in the tropics, p. 41, https://doi.org/10.21957/e34xwhysw, 1994.

30   Pringle, K. J., Tost, H., Message, S., Steil, B., Giannadaki, D., Nenes, A., Fountoukis, C., Stier, P., Vignati, E., and Lelieveld, J.: De-scription and evaluation of GMXe: a new aerosol submodel for global simulations (v1), Geoscientific Model Development, 3, 391, https://doi.org/10.5194/gmd-3-391-2010, 2010a.

Pringle, K. J., Tost, H., Metzger, S., Steil, B., Giannadaki, D., Nenes, A., Fountoukis, C., Stier, P., Vignati, E., and Lelieveld, J.: Corrigendum to "Description and evaluation of GMXe: a new aerosol submodel for global simulations (v1)" published in Geosci. Model Dev., 3,
35   391-412, 2010, Geoscientific Model Development, 3, 413, https://doi.org/10.5194/gmd-3-413-2010, 2010b.

Randerson, J., van der Werf, G., Giglio, L., Collatz, G., and Kasibhatla, P.: Global Fire Emissions Database, Version 3 (GFEDv3.1), https://doi.org/10.3334/ORNLDAAC/1191, 2013.

Sander, R., Baumgaertner, A., Cabrera-Perez, D., Frank, F., Gromov, S., Grooß, J.-U., Harder, H., Huijnen, V., Jöckel, P., Karydis, V. A., Niemeyer, K. E., Pozzer, A., Riede, H., Schultz, M. G., Taraborrelli, D., and Tauer, S.: The community atmospheric chemistry box model CAABA/MECCA-4.0, Geoscientific Model Development, 12, 1365–1385, https://doi.org/10.5194/gmd-12-1365-2019, 2019.

Stier, P., Feichter, J., Kinne, S., Kloster, S., Vignati, E., Wilson, J., Ganzeveld, L., Tegen, I., Werner, M., Balkanski, Y., Schulz, M., Boucher, O., Minikin, A., and Petzold, A.: The aerosol-climate model ECHAM5-HAM, Atmospheric Chemistry and Physics, 5, 1125–1156, https://doi.org/10.5194/acp-5-1125-2005, 2005.

Tiedtke, M.: A Comprehensive Mass Flux Scheme for Cumulus Parameterization in Large-Scale Models, Monthly Weather Review, 117, 1779–1800, https://doi.org/10.1175/1520-0493(1989)117<1779:ACMFSF>2.0.CO;2, 1989.

Tost, H., Jöckel, P., Kerkweg, A., Sander, R., and Lelieveld, J.: Technical note: A new comprehensive SCAVenging submodel for global atmospheric chemistry modelling, Atmospheric Chemistry and Physics, 6, 565–574, https://doi.org/10.5194/acp-6-565-2006, 2006a.

Tost, H., Jöckel, P., and Lelieveld, J.: Influence of different convection parameterisations in a GCM, Atmospheric Chemistry and Physics, 6, 5475–5493, https://doi.org/10.5194/acp-6-5475-2006, 2006b.

Tsimpidi, A. P., Karydis, V. A., Pozzer, A., Pandis, S. N., and Lelieveld, J.: ORACLE (v1.0): module to simulate the organic aerosol composition and evolution in the atmosphere, Geoscientific Model Development, 7, 3153–3172, https://doi.org/10.5194/gmd-7-3153-2014, 2014.

Tsimpidi, A. P., Karydis, V. A., Pozzer, A., Pandis, S. N., and Lelieveld, J.: ORACLE 2-D (v2.0): an efficient module to compute the volatility and oxygen content of organic aerosol with a global chemistry–climate model, Geoscientific Model Development, 11, 3369–3389, https://doi.org/10.5194/gmd-11-3369-2018, 2018.

Vignati, E., Wilson, J., and Stier, P.: M7: An efficient size-resolved aerosol microphysics module for large-scale aerosol transport models, Journal of Geophysical Research: Atmospheres, 109, D22 202, https://doi.org/10.1029/2003JD004485, 2004.
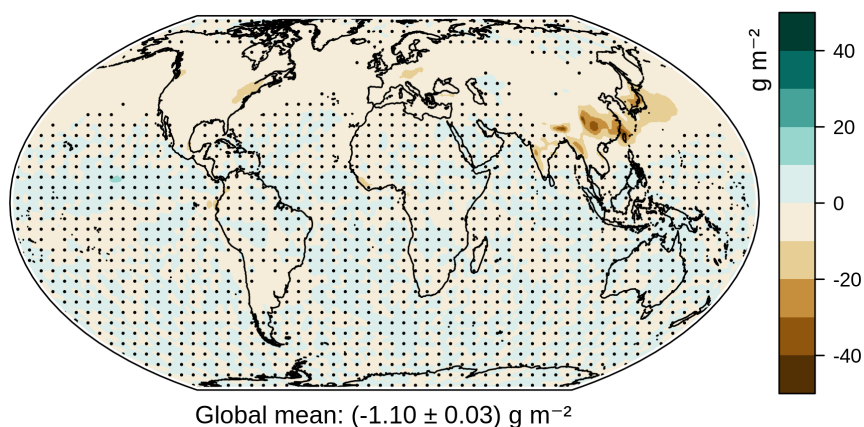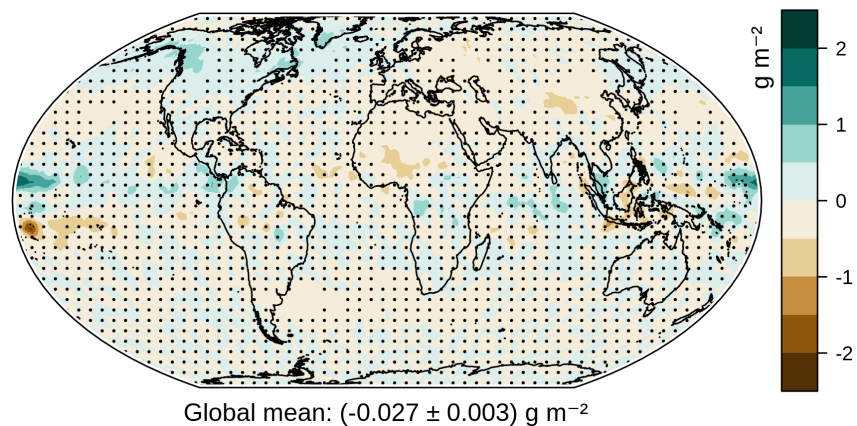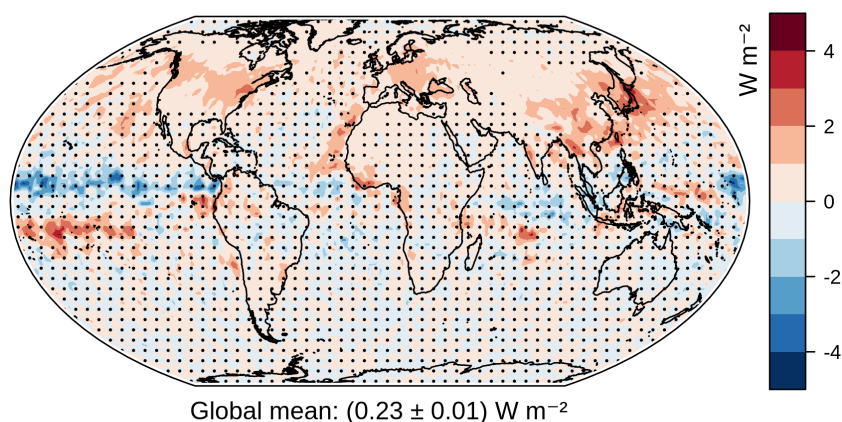
Figure 1. Annual mean effect of the dust-pollution interactions on the liquid (a) and ice (b) cloud water, calculated by applying Eq. (2) to the results of the nudged simulations. Over stippled regions the results are consistent with zero at $2\,\sigma$ significance level.

Dust-pollution interaction effect on the indirect aerosol TOA forcing

(a) Solar spectrum (SW)

Global mean: (0.23 ± 0.01) W m⁻²

(b) Terrestrial spectrum (LW)
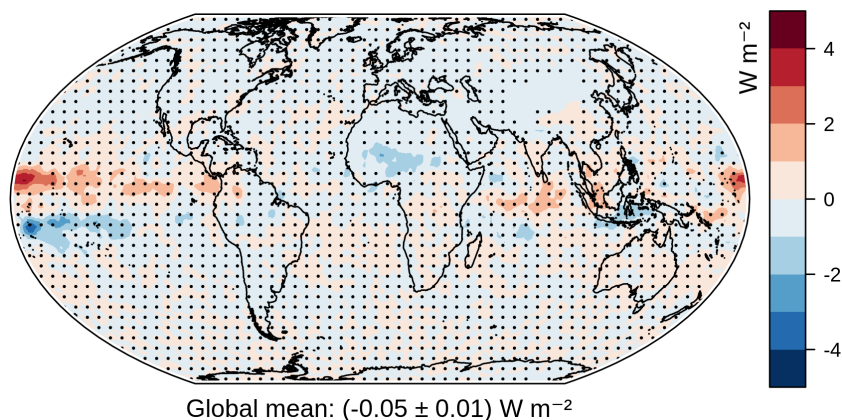

Global mean: (-0.05 ± 0.01) W m⁻²

Figure 2. Annual mean indirect effect of the dust-pollution interactions on the solar (a) and terrestrial (b) radiative forcing at the top of the atmosphere, calculated by applying Eq. (2) to the results of the nudged simulations. Over stippled regions the results are consistent with zero at 2 σ significance level.
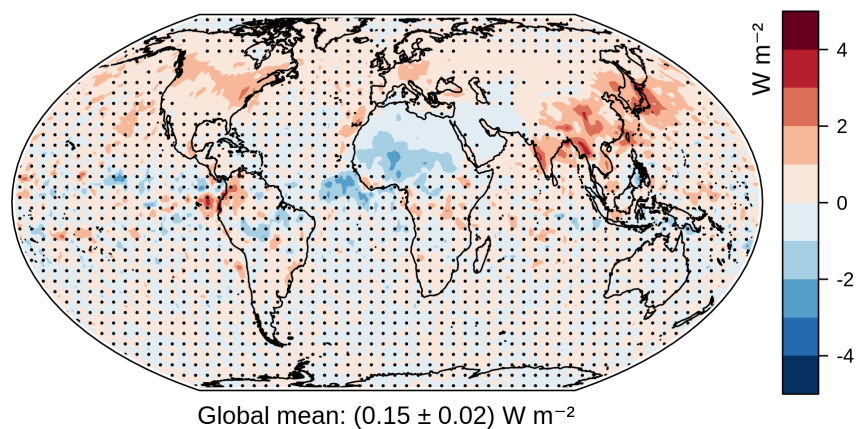
Figure 3. Total (direct and indirect, SW and LW) annual mean effect of the dust-pollution interactions on the radiative forcing at the top of the atmosphere, calculated by applying Eq. (2) to the results of the nudged simulations. Over stippled regions the results are consistent with zero at $2\,\sigma$ significance level.

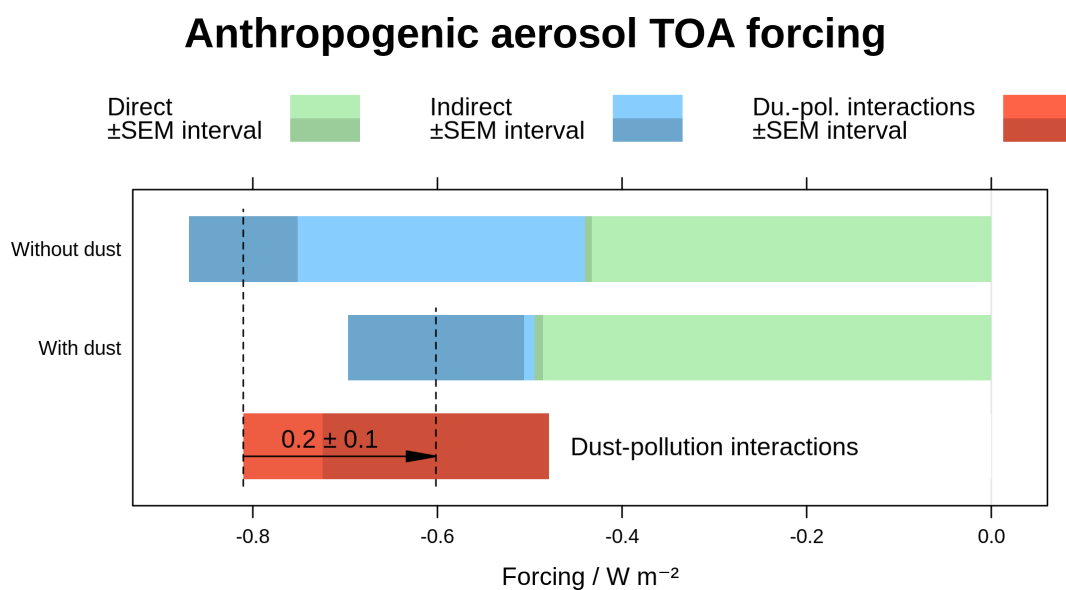**Figure 4.** Estimates of the global anthropogenic aerosol forcings at the top of the atmosphere (TOA) in the presence or absence of aeolian dust, based on the SST simulations. The total forcings comprise the direct (green) and indirect (blue) forcings. The change caused by including mineral dust corresponds to the positive forcing of dust-pollution interactions (red). Darker colours represent the standard error of mean (SEM).

Table 1. Globally averaged annual mean cloud properties and contributions thereto, based on the SST simulations. "Total" represents the simulation with all emissions, "Mineral dust" and "Anthropogenic pollution" include the effect of dust-pollution interactions ($\Delta_{\text{dust}}x + \Delta_{\text{int}}x$ and $\Delta_{\text{pol}}x + \Delta_{\text{int}}x$ in Eq. (1)), "Dust-pollution interactions" are given by the interaction term $\Delta_{\text{int}}x$, Eq. (2). The corresponding results from the nudged simulations are provided in Table S4 in the supplement.

	Total	Mineral dust	Anthropogenic pollution	Dust-pollution interactions
Droplet number / m^{-2}	$(5.845 \pm 0.009) \times 10^{10}$	$(-2.2 \pm 0.1) \times 10^9$	$(5.1 \pm 0.1) \times 10^9$	$(-2.2 \pm 0.1) \times 10^9$
Liquid water path / $(g\,m^{-2})$	85.5 ± 0.1	-1.5 ± 0.1	1.6 ± 0.2	-1.5 ± 0.2
Ice water path / $(g\,m^{-2})$	14.70 ± 0.01	-0.04 ± 0.02	0.60 ± 0.02	-0.02 ± 0.03

Table 2. Globally averaged annual mean TOA ERFs in W m^{-2}, based on the SST simulations. "Mineral dust" and "Anthropogenic pollution" include the effect of dust-pollution interactions ($\Delta_{\text{dust}}x + \Delta_{\text{int}}x$ and $\Delta_{\text{pol}}x + \Delta_{\text{int}}x$ in Eq. (1)), "Dust-pollution interactions" are given by the interaction term $\Delta_{\text{int}}x$, Eq. (2). The corresponding forcings obtained from the nudged simulations are provided in Table S4 in the supplement.

		Mineral dust	Anthropogenic pollution	Dust-pollution interactions
	Total	-0.01 ± 0.07	-0.6 ± 0.1	0.2 ± 0.1
Net	Direct	-0.260 ± 0.006	-0.490 ± 0.005	-0.054 ± 0.005
	Indirect	0.25 ± 0.07	-0.1 ± 0.1	0.3 ± 0.1
	Total	-0.04 ± 0.06	-0.86 ± 0.06	0.3 ± 0.1
SW	Direct	-0.367 ± 0.007	-0.527 ± 0.005	-0.058 ± 0.005
	Indirect	0.33 ± 0.07	-0.33 ± 0.06	0.3 ± 0.1
	Total	0.03 ± 0.08	0.26 ± 0.07	-0.07 ± 0.09
LW	Direct	0.107 ± 0.001	0.0368 ± 0.0009	0.004 ± 0.001
	Indirect	-0.08 ± 0.08	0.22 ± 0.07	-0.08 ± 0.09